1-1-2017

Crustal Cooling In The Neutron Star Low-Mass X-Ray Binary Ks 1731–260

Rachael Lynn Merritt
Wayne State University,

Recommended Citation

Merritt, Rachael Lynn, "Crustal Cooling In The Neutron Star Low-Mass X-Ray Binary Ks 1731–260" (2017). *Wayne State University Theses*. 577.
https://digitalcommons.wayne.edu/oa_theses/577

Crustal cooling in the neutron star low-mass X-ray binary KS 1731−260

by

Rachael L. Merritt

THESIS

Submitted to the Graduate School
of Wayne State University
in partial fulfillment of the requirements
for the degree of

MASTER OF SCIENCE
2017

MAJOR: Physics
Approved by:

Advisor

ACKNOWLEDGEMENTS

I would like to thank my advisor, Professor Edward Cackett. Working with him has been an incredible learning experience and has set me on a path to being a successful scientist. I would also like to thank my collaborators Edward Brown, Dany Page, Andrew Cumming, Nathalie Degenaar, Alex Deibel, Jeroen Homan, Jon Miller, and Rudy Wijnands for their invaluable input to the analysis. A big thank you to my committee members, Professors David Cinabro and Abhijit Majumder.

Finally, I would like to thank everyone in the Department of Physics and Astronomy for making my journey at Wayne State an enjoyable one.

Table of Contents

List of Tables

List of Figures

Chapter 1

Neutron Stars: An Introduction

Neutron stars provide a laboratory to study some of the densest matter in the Universe. The average neutron star density is on the order of the nuclear saturation density, ρ_o. Doing a simple calculation assuming canonical neutron star mass and radius values of 1.4 $M_\odot$ (1 $M_\odot = 1.99 \times 10^{30}$ kg) and 10 km and nucleon mass and radius values to be 1.67×10^{-27} kg and 1.2 fm (Das & Ferbel, 2003), both densities are on the order of 10^{14} g cm^{-3}. While the neutron star does not have uniform density throughout, unique effects begin happening at densities ranging from fractions of to many times ρ_o (see Section 1.2 and Figure 1.3).

Neutron star matter also has a special place on the nuclear phase diagram, as seen in Figure 1.1). Plotting temperature, T(K), versus quark chemical potential, μ(MeV), neutron star matter exists on the opposite side of the plot from matter formed in heavy ion collisions with high center-of-mass energy. The matter created in high energy heavy ion collisions is found at high temperatures with low quark chemical potential, while neutron star matter is found at low temperatures with higher chemical potential. Unlike matter produced in heavy ion collisions, the matter found in neutron star cores cannot be created in terrestrial experiments. Neutron star matter also experiences superfluidity and superconductivity. These effects can influence neutron star processes, such as crustal cooling (see Chapter 2).

The unique nuclear properties of neutron stars make them singularly important in exam-

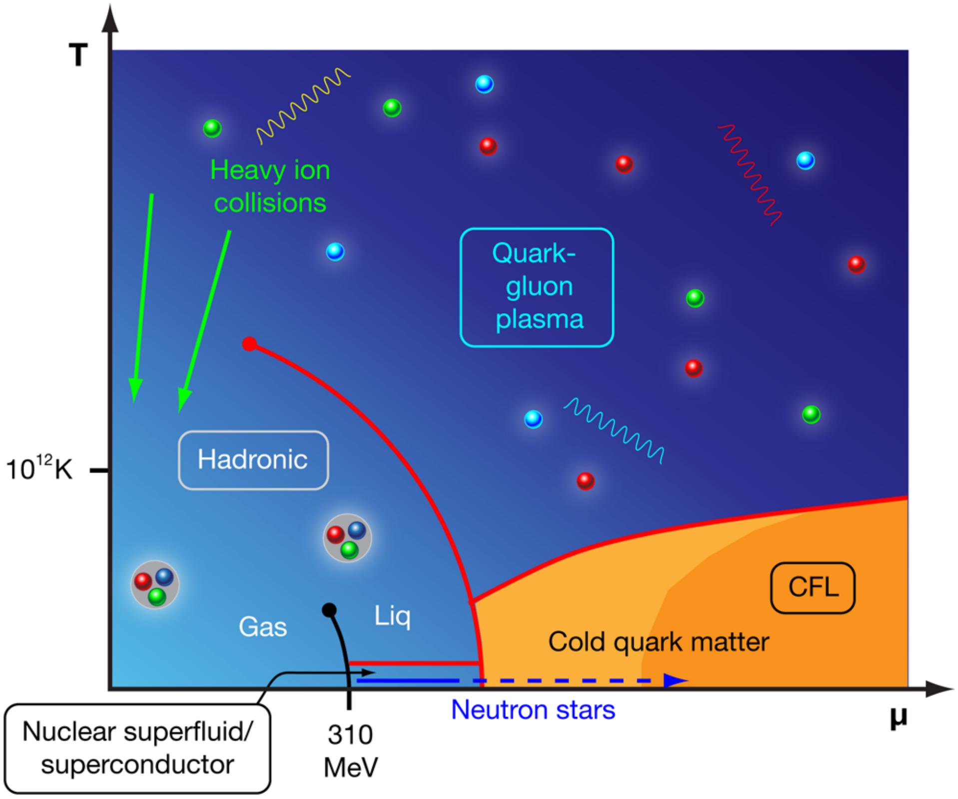

Figure 1.1: Phase diagram of nuclear matter. Just as water can go through different phases based on surroundings, given extreme enough condition nuclear matter can also be pushed into different phases. Phase transitions can be seen by plotting temperature, T(K), versus quark chemical potential, μ(MeV). Two extreme phases of nuclear matter can be seen at opposite ends of the plot. Matter created in high energy heavy ion collisions exists at high temperatures and low chemical potential while neutron star matter exists at low temperatures with high chemical potential. Image courtesy of Alan Stonebraker.

ining and understanding very dense, cold nuclear matter. Neutron stars are also an important step in stellar evolution. While they are stellar remnants, the formation of neutron stars and the fact that they still undergo active processes, like accretion, provide additional avenues of study beyond the main-sequence lifetime.

1.1 Formation of Neutron Stars

Stars will spend the majority of their lifetime as a main-sequence star, fusing hydrogen into helium. Once the hydrogen is exhausted, stars will begin other fusion processes depending on their mass. Stars with masses greater than 8 $M_\odot$ are able to fuse elements until their core becomes iron. Iron has an extremely high binding energy per nucleon and the star is unable to fuse any further, resulting in a core-collapse supernova. The core of the star contracts, causing the electrons to become a degenerate gas. In smaller stars, the degeneracy pressure of the electrons is able to equilibrate with gravity, resulting in a white dwarf. However, in massive stars, the mass of the core defeats the electron degeneracy pressure, causing the core to continue to contract. The contraction of the core increases the temperature, causing photodisintegration of iron atoms. The photodisintegration of the iron results in the production of helium atoms, neutrons, and releases 124 MeV of energy per iron atom (Prialnik, 2010).

$$\gamma +^{56}\mathrm{Fe} \rightarrow 13\ {}^{4}\mathrm{He} + 4\ \mathrm{n} - 124\ \mathrm{MeV} \tag{1.1}$$

The release of energy causes a further increase in temperature as the core continues to contract. This results in the destruction of the helium atoms and the free protons and electrons form additional neutrons, creating a neutron core. As the star continues to collapse, the neutron gas becomes degenerate and is able to halt the collapse, resulting in a neutron star.

1.2 Structure of Neutron Stars

While neutron stars have canonical radius and mass values of 10 km and 1.4 $M_\odot$, theoretically the radius and mass could vary between 8-16 km and 1-3 $M_\odot$ (Lattimer & Prakash, 2004). The star is surrounded by an atmosphere, followed by a layered envelope, a crust, and core (see Figure 1.2). The atmosphere is expected to be made of a singular light element, typically hydrogen. Due to the extreme gravity, the heavier elements sink to deeper layers of the star and the remaining atmosphere is compressed to a thickness range of 0.1 - 10 cm (Zavlin & Pavlov, 2002). The atmosphere plays a vital role in modeling the NS spectra (see Section 1.3) as this is where the photons emerge from. The few hundred meters below the

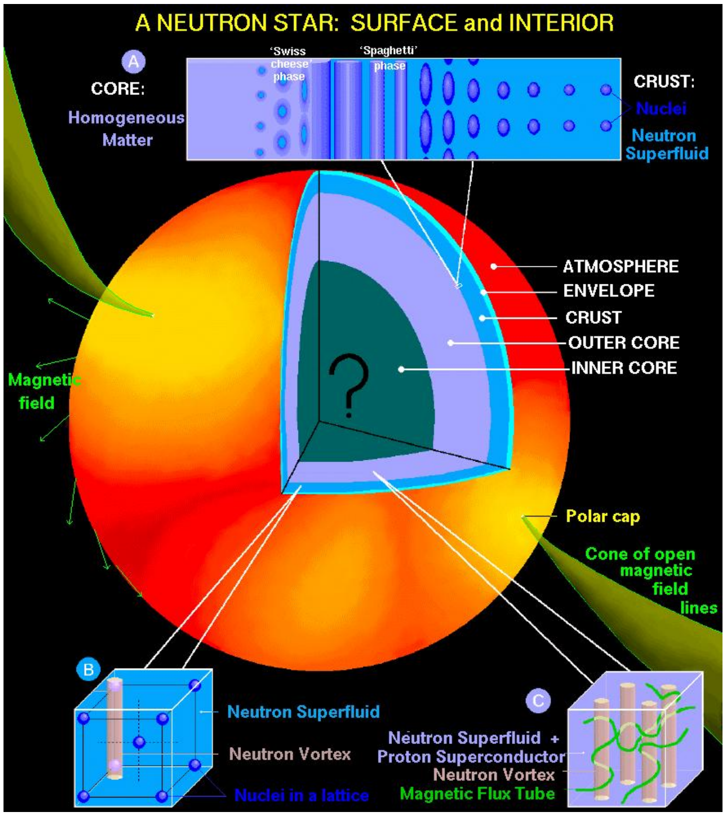

Figure 1.2: The major regions and relative sizes of regions within a neutron star. Side notes on the top and bottom of the image show the internal structure for the pasta layer in the crust of the star and for neutron superfluidity and proton superconductivity in the crust and inner core. Image courtesy of D. Page

atmosphere is the envelope. The envelope of the neutron star consists of a layer of light elements (He) on top of a layer of heavier elements (Fe) (Brown & Cumming, 2009). The 1-2 km following the envelope is a solid crust. The composition of the crust changes with depth. The outer crust consists mostly of a single atomic species, most likely iron, organized in a body-centered cubic lattice (Haensel & Zdunik, 1990). Surrounding the lattice are electron and possibly neutron gases. Once the density of the crust reaches $\sim 4\times10^{11}$ g cm^{-3}, the nuclei begin to experience neutron drip. At this density, neutrons begin to "leak" out of the nuclei, resulting in the formation of isotopes. The presence of new isotopes could possibly distort or change the lattice structure of the crust from body-centered cubic to face-centered

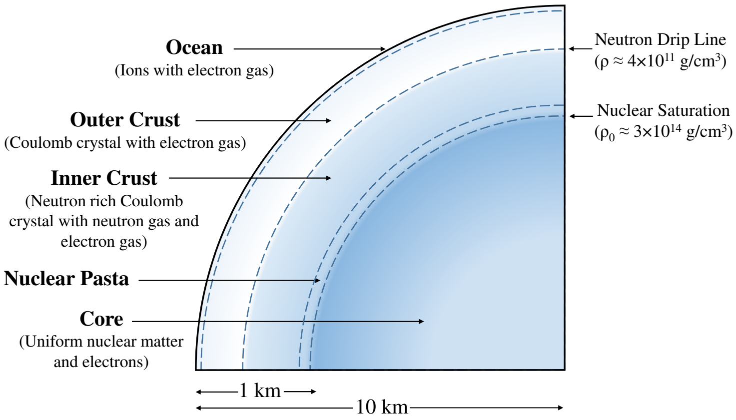

Figure 1.3: Neutron star cross section with densities from Caplan & Horowitz (2016). Neutron drip density marks the transition between the outer and inner crusts. A nuclear pasta layer is expected to exist at the base of the inner crust. The transition density between crust and core is on the order of nuclear saturation density.

cubic (Kobyakov & Pethick, 2014; Caplan & Horowitz, 2016). The now free neutrons form a neutron gas. The nuclear drip line also marks the transition between the outer and inner crusts (see Figure 1.3). As the density increases the neutrons become superfluid and Coulomb interactions become important. At nuclear saturation density, which occurs near the base of the inner crust, the nuclei are being compressed very close together - possibly touching. The force from Coulomb repulsion begins to deform the nuclei into a phase known as nuclear pasta (Caplan & Horowitz, 2016)[1]. Configurations of the deformation can be produced through molecular dynamics (MD) simulations (see Figure 1.4). The nuclei are deformed into tubes and sheets, resulting in this phase of matter being called nuclear pasta. Due to the high density at the base of neutron star crusts, a nuclear pasta phase is expected to exist (e.g., see Horowitz et al. (2015) and references therein). Pons et al. (2013) suggested that the irregular shapes in the pasta would lead to low thermal conductivity. Through modeling, there appears to be a low thermal conductivity layer at the base of the crust, consistent with nuclear pasta (Horowitz et al., 2015). The presence of a low thermal conductivity layer would influence the heating of and subsequent cooling of the neutron star

---

[1] In this phase, the nuclei are deformed into shapes that resemble different types of noodles (e.g. tubes=spaghetti and sheets=lasagna), hence the name nuclear pasta!

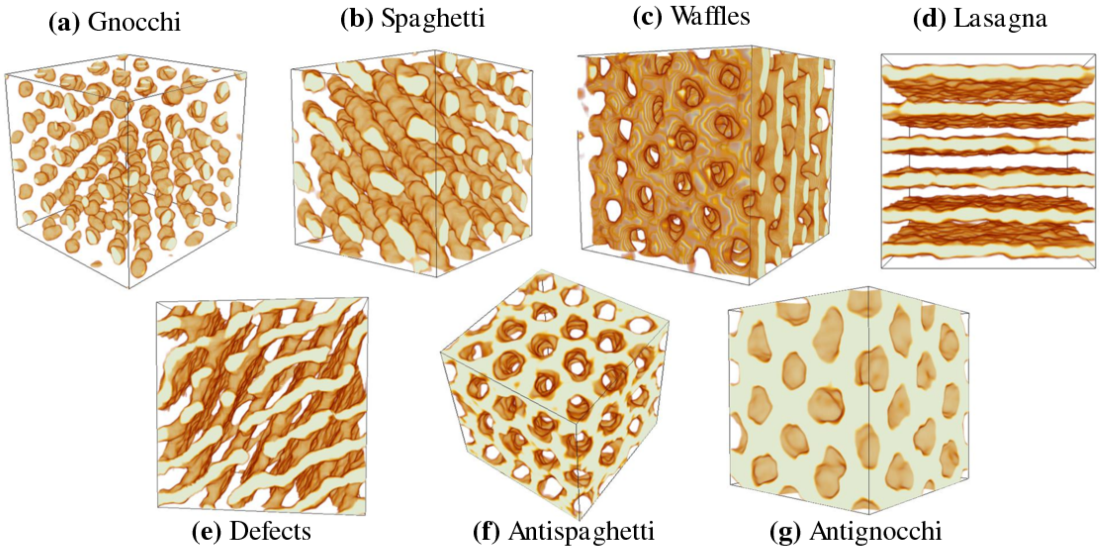

Figure 1.4: Nuclear pasta configurations produced in molecular dynamics simulations with 51,200 nucleons. For more detailed description of MD simulations, see Schneider et al. (2013, 2014); Horowitz et al. (2015)

crust. These effects will be discussed in Chapter 2. The remainder of the star is the core. The outer core of the neutron star consists of muons, electrons, and nucleons - with possible superfluidity of the neutrons and protons (Lattimer & Prakash, 2004). The goings-on of the inner core are a bit of a mystery. While it may simply be superfluid neutrons, there are suggestions of the presence of strangeness-bearing matter, such as Bose (kaon) condensates or hyperons (Λ and Σ^-), or unconfined quarks (Prakash et al., 1996). For now though, the composition of the inner crust remains an unknown.

1.3 Neutron Star Low Mass X-ray Binaries (LMXB)

Following its formation, a neutron star may still have a companion object. A low-mass X-ray binary system consists of a neutron star (or stellar mass black hole) and a companion object. To be considered low-mass, the companion needs to be less than $M_\odot$. Transient LMXBs alternate between periods of outburst, i.e. active accretion, and quiescence when

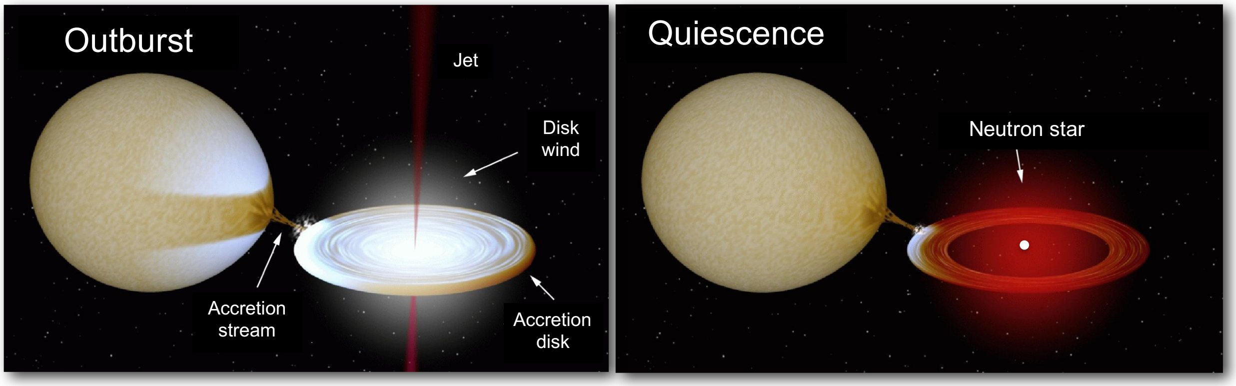

Figure 1.5: LMXB outburst versus quiescence. During outburst (left image), the X-ray emission of the neutron star is overwhelmed by the emission of the accretion disk. The system is also influenced by disk winds and jets. In quiescence (right image), the X-ray emission of the neutron star is directly observable. There is a several order of magnitude difference between outburst luminosity ($\sim 10^{36}$-10^{39} erg s^{-1}) and quiescent luminosity ($< 10^{34}$ erg s^{-1}). Image courtesy of R. Hynes

accretion rates drop significantly. The difference between outburst and quiescence can be seen in Figure 1.5). Accretion begins when the companion overflows its Roche lobe, causing material to flow from the companion toward the neutron star, forming an accretion disk around the neutron star. During outburst, the system's X-ray emission is dominated by the accretion disk and a boundary layer that forms between the inner accretion disk and neutron star surface. While in outburst, the luminosity of the system can range between 10^{36}-10^{39} erg s^{-1} (Turlione et al., 2015). Transient behavior in low-mass X-ray binaries is caused by low mass accretion rates between the donor star and the compact object (Frank et al., 2002). The mass accretion rate is not high enough to keep the system in constant outburst. Once the system returns to quiescence, the luminosity decreases to $<10^{34}$ erg s^{-1} and the thermal X-ray emission below a few keV originates from the surface of the neutron star (Brown et al., 1998). Transitions between outburst and quiescence do not happen on regular intervals and vary from source to source. Figure 1.6 shows the light-curves of three NS LMXBs (XTE J1806−246, MXB 1730−335, and MXB 1659-29) taken by the All-Sky Monitor (ASM) instrument on the Rossi X-ray Timing Explorer (RXTE). Comparing these three sources demonstrates the extreme variety in the periods of outburst and quiescence.

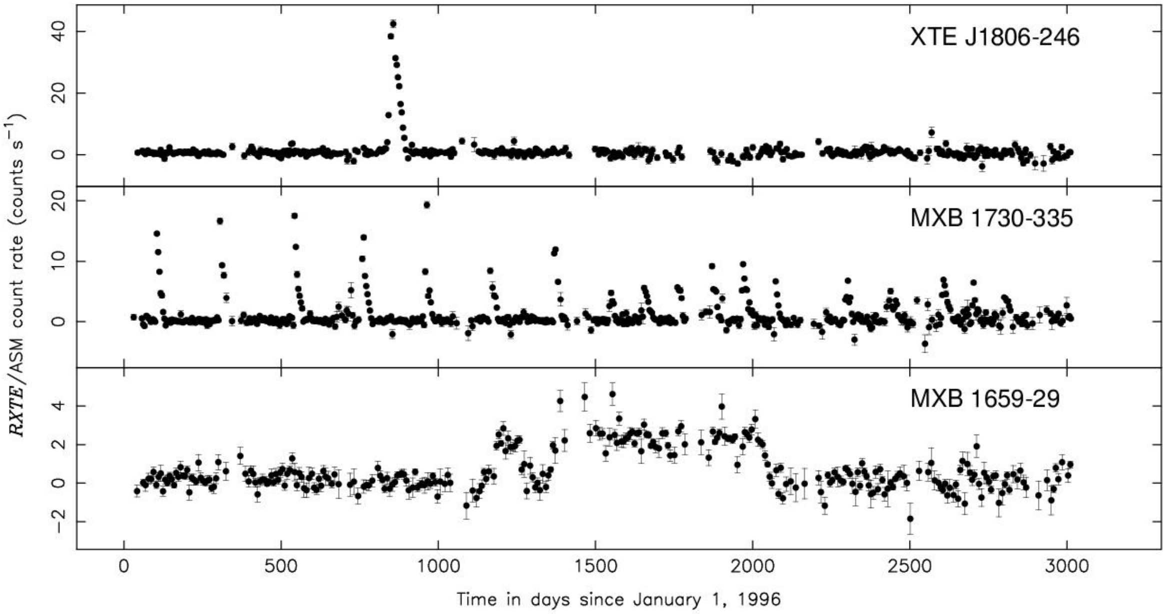

Figure 1.6: Light-curves of transient LMXBs XTE J1806−246, MXB 1730−335, and MXB 1659-29. Data taken by RXTE/ASM over 3000 day period beginning January 1, 1996.

Over a period of 3000 days (∼8 years), XTE J1806−246 experiences one outburst, lasting just a few weeks, and otherwise is in quiescence through the whole time interval. MXB 1730−335 undergoes more than 15 outbursts during the same time period. The third source, MXB 1659-29, only undergoes one period of outburst, but it lasts for nearly 3 years.

While the quiescent LMXB spectrum is predominantly thermal (with a temperature of $\sim 10^6$ K), it is not a blackbody. There is a shift of the high energy tail of the spectrum due to the atmosphere of the star (e.g. Rutledge et al. (2002)). Assuming a hydrogen atmosphere, the peak of the emission is shifted due to the frequency dependence of the opacity of free-free absorption happening in the atmosphere. This leads to higher energy photons emerging from deeper, hotter layers of the atmosphere, modifying the emission spectrum away from a simple blackbody. This can be seen in Figure 1.7. Other influences on NS atmospheric emission are gravitational effects and the depth of the thermal emission. When modeling NS atmospheres, effects from general relativity need to be considered. To correct for this, a gravitational redshift parameter is introduced when calculating the effective temperature

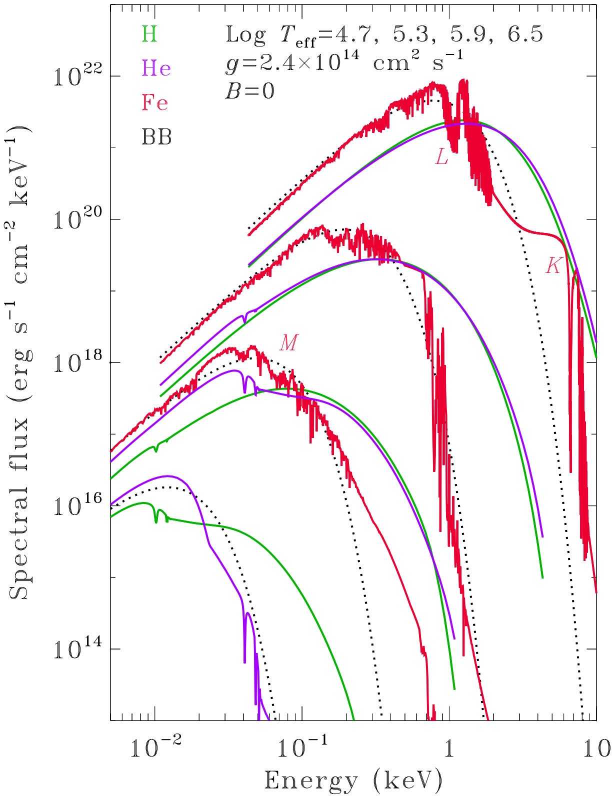

Figure 1.7: The spectral flux of thermal radiation in NS atmosphere models at different effective temperatures from Zavlin & Pavlov (2002). The dotted-black line is a normal blackbody. The solid green line is a hydrogen atmosphere. The solid purple line is a helium atmosphere. The solid red line is a iron atmosphere. All models were done with a non-magnetic atmosphere.

for an observer at infinity, where the gravitational redshift parameter is defined as:

$$g_r = \sqrt{1 - 2.952\frac{M_{NS}}{R_{NS}}} \tag{1.2}$$

$\mathrm{M_{NS}}$ and $\mathrm{R_{NS}}$ are the respective mass and radius of the neutron star (Zavlin et al., 1996). The thermal emission also changes with depth. As the depth of the surface layer increases, so does the temperature. This can be seen in Figure 1.8.

Some quiescent LMXBs show a power-law component in their spectra, in addition to the neutron star atmosphere. This power-law component may be due to residual accretion interacting with the star's magnetosphere (e.g. Campana et al. (1998); Cackett et al. (2010b);

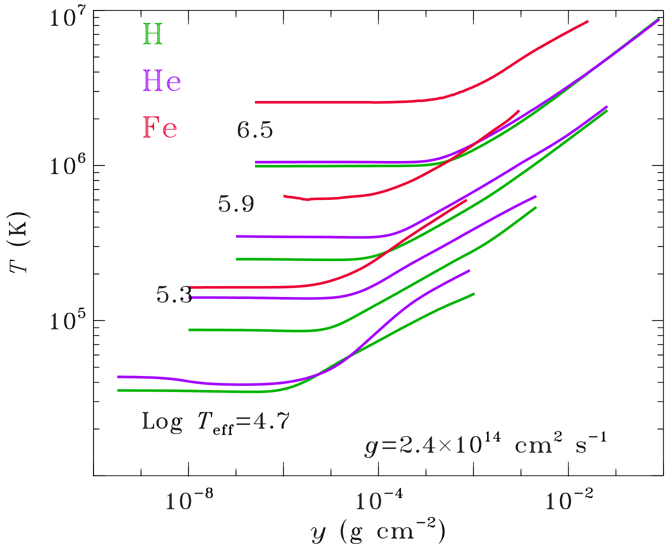

Figure 1.8: The dependence of temperature based on depth of the NS surface layer from Zavlin & Pavlov (2002). The solid green line is a hydrogen atmosphere. The solid purple line is a helium atmosphere. The solid red line is a iron atmosphere. All models were done with a non-magnetic atmosphere.

Bernardini et al. (2013)). It is also possible that the power-law component is caused by a shock from pulsar winds (Bogdanov et al., 2005).

1.4 Crustal Cooling of NS LMXBs

Accretion onto the neutron star surface can heat the stellar crust out of thermal equilibrium with the core (e.g. Ushomirsky & Rutledge (2001); Rutledge et al. (2002)). As the star is accreting, there is an increase in pressure as the material falls onto the stellar surface. As the heavier materials sink to lower depths electron capture begins to happen near the neutron drip line (ρ ~10^{11} g cm^3). This allows for the creation and absorption of neutrons, increasing the neutron-richness of the nuclear material. As densities increase ($\rho \sim 10^{12}$-10^{13} g cm^{-3}), density driven pycnonuclear fusion begins to take place in the inner crust (Haensel & Zdunik, 2008). These processes are referred to as 'deep crustal heating' (e.g. Brown et al. (1998) and can explain the observed neutron star luminosities during quiescence. The energy released from these processes heats the crust out of thermal equilibrium with the core. Once the LMXB returns to quiescence, the thermal relaxation of the crust can be observed directly.

Crustal cooling of accretion-heated neutron stars provides insight into the stellar interior of neutron stars. As time progresses, heat from within the crust diffuses to the surface. Therefore, the thermal emission observed early in quiescence relates to heat from the upper layers of the outer crust. Later in quiescence, the thermal emission is coming from deeper layers. This allows for probing the inner parts of the crust. Direct observation of crustal cooling allows for the extraction of neutron star properties, such as thermal conductivity, crustal structure, and core temperature via cooling models (Shternin et al., 2007; Brown & Cumming, 2009; Page & Reddy, 2013; Turlione et al., 2015; Deibel et al., 2015; Ootes et al., 2016). Crustal cooling of neutron star LMXBs has been observed in eight sources: KS 1731−260 (Wijnands et al., 2001, 2002; Cackett et al., 2006, 2010a), MXB 1659−29 (Wijnands et al., 2003, 2004; Cackett et al., 2006, 2008, 2013), EXO 0748−676 (Degenaar et al., 2009, 2011b, 2014; Díaz Trigo et al., 2011), XTE J1701-462 (Fridriksson et al., 2010, 2011), IGR J17480−2446 (Degenaar et al., 2011a, 2013, 2015), MAXI J0556−332 (Homan et al., 2014), Swift J174805.3−244637 (Degenaar et al., 2015), and potentially Aql X-1 (Waterhouse et al., 2016). The cooling curves of these sources generally show a significant drop in temperature immediately following their return to quiescence, typically showing a close to exponential decay, with the curves then flattening as the cooling continues (see Figure 1.9 for a comparison of several sources). However, the sources show a wide distribution of temperatures at the beginning of quiescence ($\sim$100 − 300 eV), cooling timescale (e-folding time) and outburst timescales (a few months to nearly 24 years). While it was initially thought that long (quasi-persistent) outbursts were required to heat the crust out of thermal equilibrium, the observation of crustal cooling in IGR J17480-2446, Swift J174805.3−244637 and Aql X-1 demonstrates that it can occur with outbursts of only a few months.

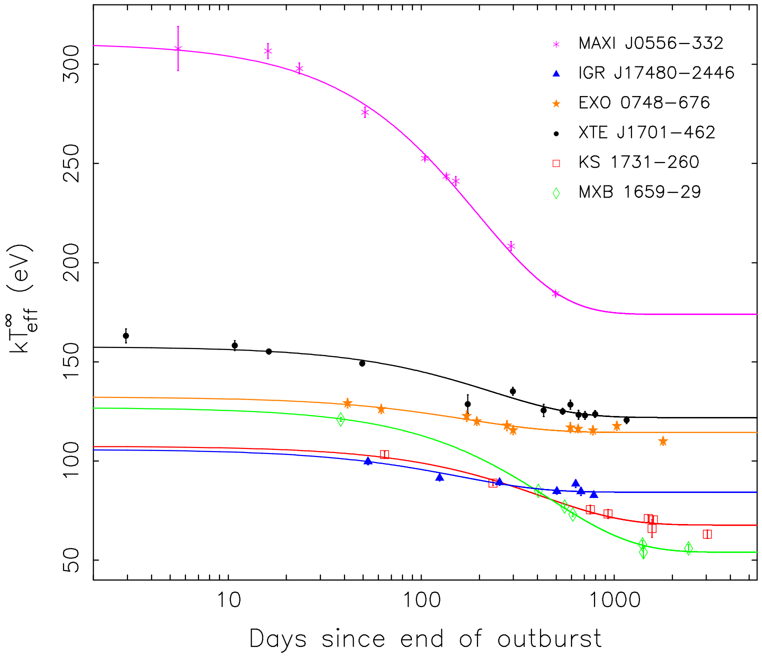

Figure 1.9: The effective temperatures of six NS LMXBs over a period of approximately 3000 days after returning to quiescence (Homan et al., 2014): MAXI J0556−332, IGR J17480−2446, EXO 0748−676, XTE J1701-462, KS 1731−260, and MXB 1659−29.

1.5 X-ray Astronomy and Spectral Analysis

Quiescent neutron stars are hot ($\sim 10^6$ K), thus studying their emission requires X-ray observations. Since the analysis presented in Chapter 2 relies on X-ray observations and analysis, it is useful to briefly review the basic concepts behind X-ray astronomy here.

High energy astrophysics focuses on extreme ultraviolet wavelengths, X-rays, and gamma rays. Fortunately for living things, these types of EM radiation do not penetrate the Earth's atmosphere and therefore cannot be observed with ground-based telescopes. Even using satellites, capturing X-rays is a difficult task. Unlike visible light, which can be directed without many problems, X-rays can easily penetrate through most materials. In order to direct the photons in a meaningful way, the mirrors are set up with small incident angles in order to utilize total external reflection. The critical angle (θ_c) for total external reflection is defined as:

$$\theta_c = \sqrt{2\delta} \tag{1.3}$$

where δ is:

$$\delta = \frac{r_e(\frac{hc}{E})^2 N_e}{2\pi} \tag{1.4}$$

In Equation 1.4, r_e is the electron radius, h is Planck's constant, c is the speed of light, and N_e is electron density (Arnaud et al., 2011). Since the number of electrons should be proportional to the number of protons in the nucleus (Z), the critical angle for total external reflection can be written as:

$$\theta_c \propto \frac{\sqrt{Z}}{E} \tag{1.5}$$

Since θ_c is proportional to $\sqrt{Z}$, current X-ray telescopes use materials with higher atomic numbers, such as gold, iridium, and platinum as reflective coating to maximize the critical angle (Arnaud et al., 2011).

The most effective mirror shapes for focusing X-rays on a detector are paraboloids and hyperboloids (see Section 1.3.2 of Arnaud et al. (2011)). This combination allows for the maximum collecting area, while dealing with the limitations of cost, weight, and the ability to put the telescope into space (Arnaud et al., 2011). Using both parabolic and hyperbolic mirrors gives an effective aperture area of

$$A = 2\pi R\alpha L \tag{1.6}$$

where R is the radius of the mirror, alpha is the incident angle of the incoming X-rays, and L is the length of the parabola (Arnaud et al., 2011). To further improve photon collection, mirrors of different radii are nested together to increase the total area for interception of the incoming X-rays (see Figure 1.10).

The detectors on X-ray telescopes need to be able to record the position, arrival time, and energy of the incoming photons. X-ray telescopes utilize a variety of detectors such as charge-couple devices (CCDs), CdZnTe detectors, and calorimeters. In this thesis I analyze data from *Chandra* and *XMM-Newton*. Both are very well calibrated to the 0.5 - 10 keV energy range. The primary detectors on these satellites are CCDs. The Advanced CCD

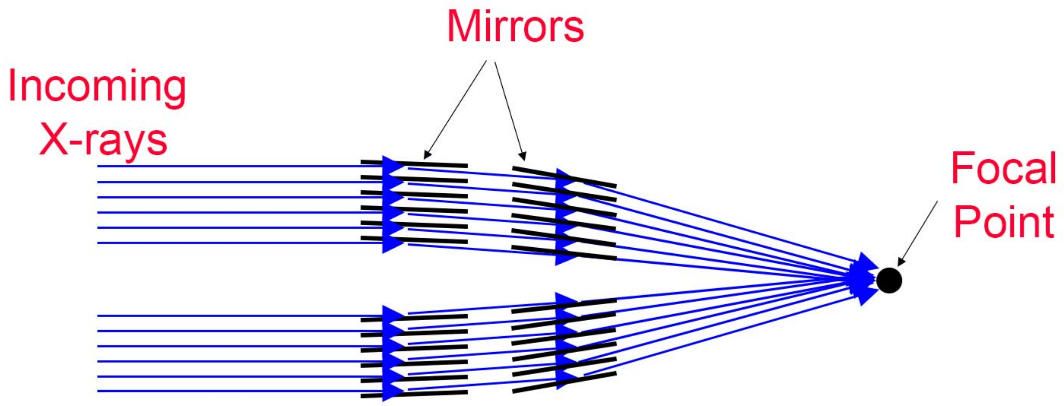

Figure 1.10: X-ray telescope schematic of nested mirrors. By nesting cylindrical mirrors at small angles, X-rays are able to graze off of the mirrors and are focused on the detector. Using multiple mirrors allows for the collection of more photons than a single mirror system. Image courtesy of NASA's Imagine the Universe.

Imaging Spectrometer (ACIS) on *Chandra* has a full width at half maximum (FWHM) energy resolution of 150 eV at 6 keV. On *XMM-Newton*, the European Photon Imaging Cameras (EPIC) have a FWHM energy resolution of 120 eV at 6.5 keV. ACIS has an on-axis effective area of 110 cm^2 at 0.5 keV, 600 cm^2 at 1.5 keV, and 40 cm^2 at 8 keV respectively. For EPIC at 1 keV, the MOS 1/2 cameras have an on-axis effective area of 922 cm^2 and the PN camera has an effective area of 1227 cm^2. For a full description of X-ray detectors, see Chapters 2 and 3 of Arnaud et al. (2011). The quantum efficiency, energy scale, and spectral resolution of the detector needs to be taken into consideration when reducing the collected data. These factors influence the systematic uncertainties when doing data reduction. Each telescope has a software package for calibrating and processing the data. Before anything meaningful can be taken from the data, it must be reprocessed with calibration files for tasks such as exposure selection and the creation of bad pixel files. Once the data has been calibrated, source and background regions are chosen. Using these regions, response files are created. The response files take the sources of systematic uncertainties (e.g. telescope area, detector efficiencies versus energy) and are then used to create the final spectrum. Specific details about data reduction used in this work can be found in Section 2.2.

1.6 Thesis Outline

This thesis focuses on the the crustal cooling observed in neutron star LMXB KS 1731−260, and the implications this has for neutron star structure. In Chapter Two, we will introduce KS 1731−260 in detail and will present a new *Chandra* observation of KS 1731−260, taken six years after the previous *Chandra* observation and a total of approximately 14.5 years into quiescence. In addition to new data, recent updates to the crust cooling model used in Brown & Cumming (2009) (see Section 2.3.2), allow for the exploration of new parameters such as the influence of a nuclear pasta layer and additional shallow heating of the crust. Our findings suggests that cooling has likely halted in KS 1731−260 and that the neutron star crust has returned to thermal equilibrium with the core. In Section 2.2 we give an overview of data reduction and spectral analysis. In Section 2.3 we discuss empirical and physical models to fit the quiescent light curve. In Chapter Three, we discuss our findings and future work.

Chapter 2

Crustal Cooling of LMXB KS 1731−260

This analysis has been published as "*The Thermal State of KS 1731−260 after 14.5 years in Quiescence*" in The Astrophysical Journal, Volume 833, Issue 2, article id. 186, 7 pp. (2016) (Merritt et al., 2016).

2.1 Introduction

KS 1731−260 was discovered by the *Mir-Kvant* instrument in August 1989 and in previous data it was also observed in outburst in October 1988 (Sunyaev et al., 1989, 1990). It remained in outburst until early 2001 (Wijnands et al., 2001). The light-curve showing the transition between outburst and quiescence can be seen in Figure 2.1. KS 1731-260 was the first source for which crustal cooling was observed and has provided the longest cooling baseline for any source to date. A detailed history of the source can be found in Cackett et al. (2006). Since returning to quiescence, monitoring observations with *Chandra* and *XMM-Newton* have shown continued cooling up until 2009 (8 years into quiescence; Wijnands et al., 2001, 2002; Cackett et al., 2006, 2010a). Physical models that track the thermal evolution of the neutron star reproduce the observed cooling in KS 1731-260 (e.g.

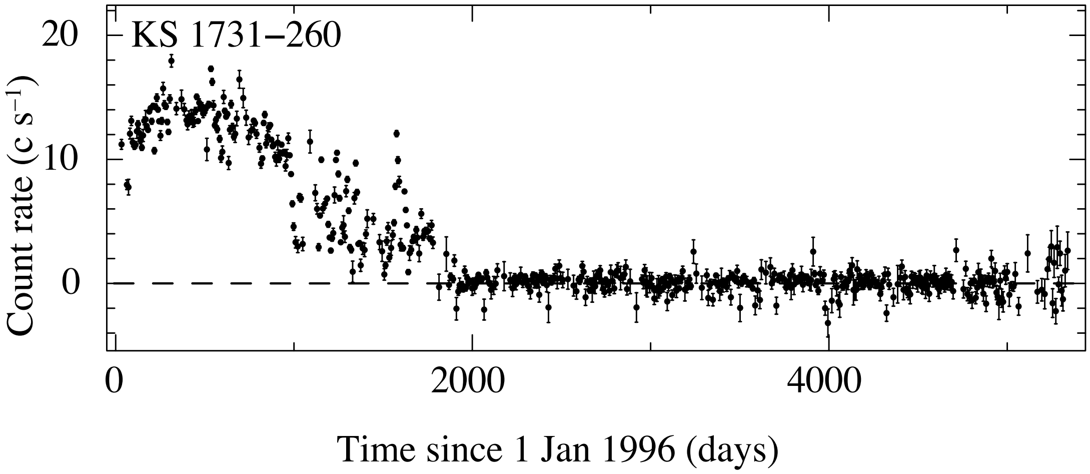

Figure 2.1: Light-curve of KS 1731−260. KS 1731−260 returned to quiescence in early 2001. Data taken by RXTE/ASM.

Shternin et al., 2007; Brown & Cumming, 2009; Page & Reddy, 2013; Turlione et al., 2015; Ootes et al., 2016). Fits to the crustal cooling of KS 1731-260 consistently suggest that the crust has a high thermal conductivity indicating a low impurity parameter (i.e. an ordered lattice crustal structure; see below). Moreover, in order to match the early evolution in the cooling curves it has been found that an additional source of heating at shallow depths in the crust is often needed (e.g., Brown & Cumming, 2009; Degenaar et al., 2011a; Deibel et al., 2015; Waterhouse et al., 2016). Such shallow heating is also required in order to provide the conditions for superburst ignition (Cumming et al., 2006; Gasques et al., 2007). A superburst is a Type I X-ray burst caused by carbon burning in the crust. Superbursts can last for up to a day.

Here we present the a new *Chandra* observation of KS 1731−260, taken approximately 14.5 years into quiescence. We give an overview of data reduction and spectral analysis and discuss empirical and physical models to fit the quiescent light curve.

2.2 Data Reduction and Analysis

The new *Chandra* observation of KS 1731−260 was performed over 150 ks in three separate pointings. A 66 ks segment was performed on 2015 August 6/7 (ObsID: 16734). A 20 ks segment was performed on 2015 August 8 (ObsID: 17706) and 64 ks segment was performed on 2015 August 9 (ObsID: 17707). As with the previous *Chandra* observations, KS 1731−260 was at the default aimpoint of the ACIS-S3 chip. Due to the time since the previous *Chandra* and *XMM-Newton* observations, we decided to reanalyze all data with the latest calibration files and software. Full details on the previous observations can be found in Wijnands et al. (2001, 2002); Cackett et al. (2006, 2010a), and also see Table 2.1.

Observation ID	MJD	$kT_{\mathrm{eff}}{}^{\infty}$ (eV)	F_{obs} (10^{-15} ergs cm^{-2} s^{-1})	L_{bol} (10^{33} ergs s^{-1})
2428 (CXO)	51995.1	104.6 ± 1.3	$41.6 \pm ^{3.4}_{3.6}$	2.69
013795201/301 (XMM)	52165.7	89.5 ± 1.03	$16.1 \pm ^{1.10}_{0.97}$	1.47
3796 (CXO)	52681.6	76.4 ± 1.8	$5.98 \pm ^{0.71}_{0.91}$	0.76
3797 (CXO)	52859.5	73.8 ± 1.9	$4.79 \pm ^{0.58}_{0.63}$	0.64
0202680101 (XMM)	53430.5	71.7 ± 1.4	$3.97 \pm ^{0.53}_{0.51}$	0.59
6279/5486 (CXO)	53512.9	70.3 ± 1.9	$3.49 \pm ^{0.61}_{0.41}$	0.55
10037/10911 (CXO)	54969.7	64.5 ± 1.8	$1.99 \pm ^{0.30}_{0.36}$	0.39
16734/17706/707 (CXO)	57242.1	64.4 ± 1.2	$1.97 \pm ^{0.23}_{0.22}$	0.39

Table 2.1: Neutron Star Atmosphere Fitting Parameters. Mass and radius are fixed to 1.4 $M_{\odot}$ and 10 km, respectively. Spectra were modeled using an absorbed neutron star atmosphere model (nsa) and a photoelectric absorption model (phabs). The distance to KS 1731-260 was set to 7 kpc and the column density was tied between observations, giving a best fitting value of $N_{\mathrm{H}} = 1.30 \pm 0.06 \times 10^{22}$ cm^{-2}. The effective temperature ($kT_{\mathrm{eff}}^{\infty}$) is corrected for gravitational redshift (i.e. it is the effective temperature for an observer at infinity). The ObsID and observatory are indicated in the left column of the table (CXO = *Chandra* and XMM=*XMM-Newton*). The observed flux was calculated over the 0.5-10 keV range. The bolometric luminosity was calculated over the $0.01 - 100$ keV range. We do not include errors on L_{bol} due to large systematic errors.

2.2.1 Chandra Data Reduction

We analyzed the *Chandra* data using CIAO (v 4.7) and CALDB (v 4.6.8). Following Cackett et al. (2006, 2010a) we used a 3” circular extraction region for the source and an annular extraction region for the background with a inner radius of 7” and outer radius of 25". The most recent observation had a net count rate of $3.9 \pm 0.6 \times 10^{-4}$ counts s^{-1}, which is consistent with the previous 2009 *Chandra* observation, which had a net rate of $4.8 \pm 1.0 \times 10^{-4}$ counts s^{-1}. All observations were reprocessed for the latest calibration files using the `chandra_repro` task. We used `specextract` to extract the spectra and to create the response matrices.

2.2.2 XMM Data Reduction

We analyzed the *XMM-Newton* data using *XMM* Science Analysis Software (SAS) (v 14.0.0). As with previous analyses, we used a 10" circular extraction region for the source and a 1' circular, off source extraction region for the background. We reprocessed the observation files using the `emproc` and `epproc` tasks. We used `evselect` to extract the spectra and `rmfgen` and `arfgen` to generate the response matrices. In both *XMM-Newton* observations there was significant and consistent background flaring. Due to this, we excluded any times when the >10 keV light curve had more than 2 counts s^{-1} for MOS 1 and 2 and more than 4 counts s^{-1} for the PN. We also filtered patterns $0 - 12$ for the MOS and patterns $0 - 4$ and flag=0 for the PN. The removal of the background flaring eliminated 2% of the total exposure time for MOS 1 and 2 and 10-15% of the total exposure time for the PN.

2.2.3 Spectral Analysis

We fit all available *Chandra* and *XMM-Newton* spectra since the end of outburst using XSPEC (ver. 12.9.0; Arnaud, 1996) following a procedure similar to Cackett et al. (2006, 2010a). We modeled the spectra using a neutron star atmosphere model (nsa; Zavlin et al., 1996), modified by photoelectric absorption within our Galaxy (phabs). The nsa model has been used previously in studies of KS 1731−260, and other models, such as nsatmos (Heinke et al., 2006), provide consistent results within 1σ. A comparison of atmosphere models can be found in Section 3.4 of Heinke et al. (2006). For our analysis and modeling, we fix the neutron star radius to canonical values of 10 km and the mass to 1.4 $M_{\odot}$. We set the distance

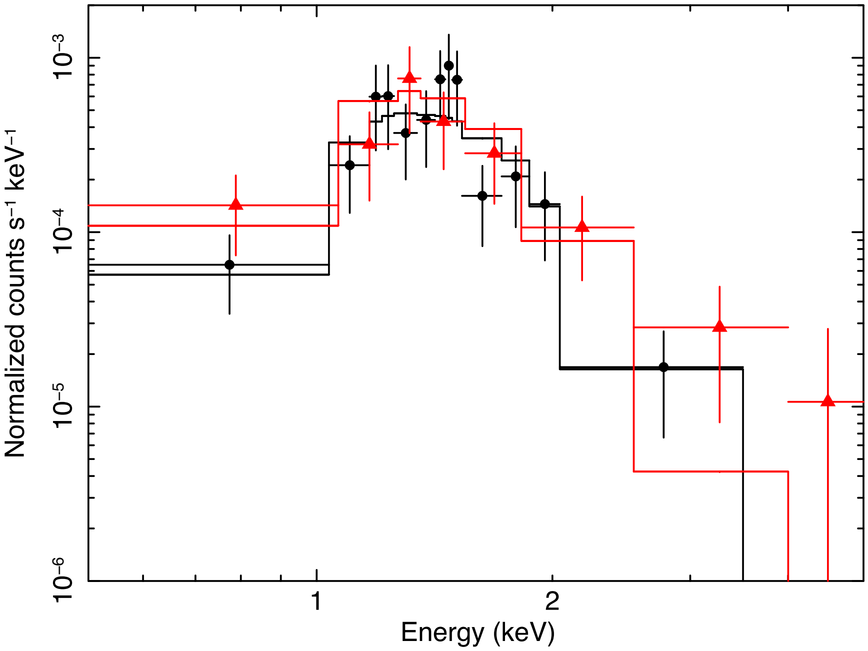

Figure 2.2: The X-ray spectrum of KS 1731−260 from the 150 ks *Chandra* observation in 2015 August (black, circles) compared to the 2009 May *Chandra* observation (red, triangles), along with the best-fitting absorbed neutron star atmosphere modeling. There is no significant change between 2009 and 2015. For purposes of clarity in this figure only we have combined separate pointings to create one spectrum for each epoch, and visually rebinned the data.

to the source at 7 kpc (Muno et al., 2000), resulting in a normalization parameter ($1/D^2$) $= 2.041 \times 10^{-8}$ pc^{-2}. The normalization is also a fixed parameter. We show the X-ray spectrum, and best-fitting model, for the new *Chandra* observation in Figure 2.2, compared to the 2009 *Chandra* observation. The latest spectrum is still thermal, with no need for an additional power-law component, and shows no significant change between 2009 and 2015 (see Figure 2.2).

All spectra were fit simultaneously with absorption column density, $N_{\rm H}$, tied between all observations and the effective temperature set as a free parameter. Due to the close proximity of some observations, several spectra had their parameters tied together. We tied the parameters of the spectra for *XMM-Newton* observations taken around MJD 52165.7 (ObsIDs 012795201/301) and *Chandra* observations taken around MJD 53512.9 (ObsIDs 6279/5468), MJD 54969.7 (ObsIDs 10037/10911), and MJD 57242.1 (ObsIDs 16734/17706/17707). Us-

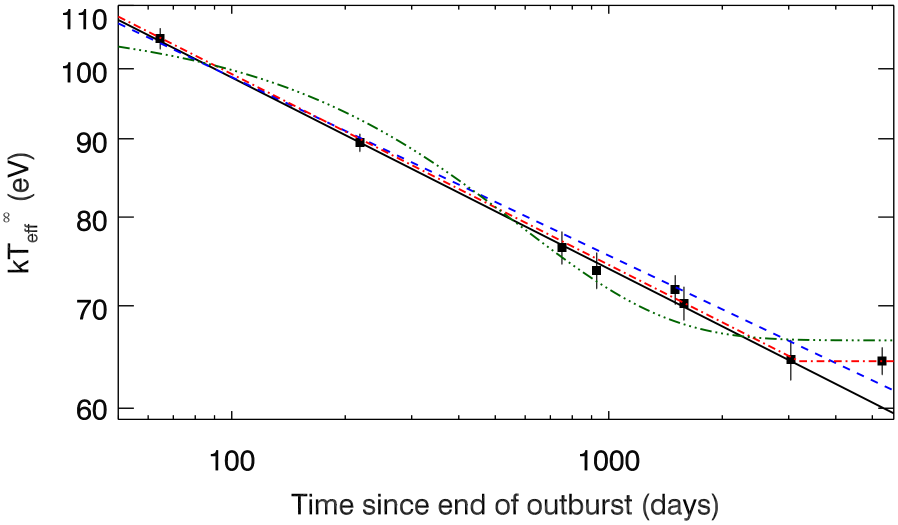

Figure 2.3: Effective temperature for KS 1731−260 over approximately 5300 days since the end of outburst. The lines indicate empirical model fits for a power-law fit to the first 7 data points, i.e. excluding the most recent one (black, solid line); a power-law fit to all 8 data points (blue, dashed line); an exponential decay to a constant (green, dash-dot-dot-dot line); a broken power-law (red, dash-dot line).

ing GRPPHA, we binned the spectra to have one count per bin. We used C-statistic to fit the binned spectra. C-statistic was used rather than χ^2 statistics due to low number of total counts in some spectra.

The spectral fitting results are shown in Table 2.1. The effective temperature is corrected for gravitational redshift (i.e. it is the effective temperature for an observer at infinity). The new *Chandra* observation gives $kT_{\rm eff}^{\infty} = 64.4 \pm 1.2$ eV, this temperature is consistent with the previous 2009 *Chandra* observation ($kT_{\rm eff}^{\infty} = 64.5 \pm 1.8$ eV) within 1σ, suggesting that the crust of KS 1731−260 has returned to thermal equilibirum with the core. The progression of effective temperature over time (cooling curve) is shown in Figure 2.3.

2.3 Cooling Curves

2.3.1 Empirical Models

Prior to the 2015 observation, the cooling curve of KS 1731−260 was well fit by a simple power-law (Cackett et al., 2008, 2010a) or an exponential decay to a constant (Cackett et al., 2006, 2010a). We fit both models to all data points (see Figure 2.3). The exponential decay to a constant (green dash-dot-dot-dot line in Fig. 2.3), provides a poor fit with $\chi^2 = 20.3$ for 5 degrees of freedom (d.o.f.), while the power-law provides a significantly better fit (blue dashed line in Fig. 2.3), with $\chi^2 = 7.76$ for 6 d.o.f. We used a power-law of the form $y(t) = \alpha(t-t_0)^\beta$, where t_0 corresponds to midday of the last observation of KS 1731−260 in outburst (MJD 51930.5, Cackett et al., 2006). The best fitting parameters are $\alpha = 169.0 \pm 0.9$ eV, and $\beta = -0.117 \pm 0.004$ eV/day. This power-law fit bisects the last two points, given that the last point has the same temperature as the previous one. We therefore also try a broken power-law model, of the form $y(t) = \alpha \left(\frac{t-t_0}{t_{\rm br}}\right)^\beta$ for $t < t_{\rm br}$ and $y(t) = \alpha$ for $t \geq t_{\rm br}$ (red, dash-dot line in Fig. 2.3). This provides a better fit, with $\chi^2 = 1.26$ for 5 d.o.f., with best fitting parameters of $\alpha = 64.4 \pm 1.2$ eV, $\beta = -0.125 \pm 0.005$ eV/day and $t_{\rm br} = 3200 \pm 600$ days. Using an F-test, this improvement in χ^2 is significant at the 2.9σ confidence level.

Given suggestions that cooling has stopped, we also fit a power-law to just the first 7 observations, i.e., excluding the latest one (see the black solid line in Fig 2.3) and get best fitting parameters $\alpha = 175.5 \pm 2.9$ eV and $\beta = -0.125 \pm 0.002$ eV/day. Extrapolating this power-law to the time of the latest observation gives $kT_{\rm eff}{}^\infty = 60.2$ eV. The measured effective temperature for the newest observation ($kT_{\rm eff}{}^\infty = 64.4 \pm 1.2$ eV) therefore deviates from the extrapolation of the previous cooling behavior at the 3.5σ level. This further suggests that the crust of KS 1731−260 may have stopped cooling.

2.3.2 Physical Models

In order to fit the quiescent crustal cooling, we model the thermal evolution of the neutron star using the open-source code `dStar`[1] (Brown, 2015). This code uses the same microphysics and integration scheme discussed in Brown & Cumming (2009). In addition, the code now has a more flexible interface that allows the distribution of heat sources and impurities with depth specified by the user; this allows us to model the effect of an additional heat source in the shallow ocean and an insulating pasta layer in the deep crust. Fixed parameters in `dStar` include the crust composition, where the composition of Haensel & Zdunik (1990) is used, the atmosphere model with the column depth of the light element layer set to $10^4\,\mathrm{g\,cm^{-2}}$, crust-core transition density of 8.13×10^{13} g cm^{-3}, and the radius and mass are set to 10 km and 1.4 $\mathrm{M}_\odot$ to be self-consistent with the spectral fits. Our `dStar` models use the superfluid critical temperature in the crust from Schwenk et al. (2003).

Prior to modeling the cooling, we simulate 12.5 years of constant accretion at the rate of $\dot{M} = 10^{17}$ g s^{-1} which is consistent with the time averaged accretion rate found by Galloway et al. (2008). For the initial run of models we varied three parameters: core temperature (T$_c$), the impurity parameter (Q$_{imp}\equiv$ n$_{ion}^{-1}\sum_i$n$_i$(Z$_i$ - $\langle$Z$\rangle$)^2) of the crust, and additional shallow heating of the crust (Q$_{sh}$). The impurity parameter measures the distribution of nuclide charge numbers. This influences the conductivity and structure of the crust (i.e. low Q$_{imp}$ means high thermal conductivity and well structured lattice). The shallow heating is an additional few MeVs of crustal heating caused by an unknown source (e.g. Cumming et al., 2006; Brown & Cumming, 2009; Medin & Cumming, 2014; Deibel et al., 2015). In the model, we set the depth of the shallow heating to occur between pressure values of $\mathrm{P}_{Q_{sh},min} = 1\times10^{27}$ g cm^{-1} s^{-2} and $\mathrm{P}_{Q_{sh},max} = 1 \times 10^{28}$ g cm^{-1} s^{-2}. The pressure values were chosen so that the heat source was shallower than the depth corresponding to the thermal time of the first observation, but otherwise it was arbitrary. The cooling curve is not that sensitive to these boundaries since the first observation is 65 days after the end of the outburst. The influence

---

[1] `https://github.com/nworbde/dStar`

of the T_c, Q_{imp} and Q_{sh} parameters on the shape cooling curve can be seen in panels (a) – (c) of Figure 2.4.

We calculate the thermal evolution of the crust for a wide range in all parameters, creating a grid of cooling curve models. This is the first time a full exploration of parameter space has been conducted. To find the best fit parameters, we search the grid to find the model which fits the data with the lowest χ^2 value. The best fitting parameters are $\mathrm{T}_c = 9.35 \pm 0.25 \times 10^7$ K, $\mathrm{Q}_{imp} = 4.4^{+2.2}_{-0.5}$, and $\mathrm{Q}_{sh} = 1.36 \pm 0.18$ MeV/nucleon. The uncertainties quoted here, and throughout the paper are at the 1σ level. The best fitting model is shown as a solid black line in Figure 2.6. This model gives a reduced-$\chi^2 = 2.00$ (d.o.f. $= 5$). Our core temperature value is approximately 2 times greater than the core temperature values found in Cackett et al. (2010a) ($\mathrm{T}_c = 4.6 \times 10^7$ K) and Brown & Cumming (2009) ($\mathrm{T}_c = 5.4 \times 10^7$). We find our impurity parameter value is higher than but similar to (Cackett et al., 2010a) ($\mathrm{Q}_{imp} = 4.0$) and approximately three times greater than Brown & Cumming (2009) ($\mathrm{Q}_{imp} = 1.5$). The slightly different core temperature is not surprising since it is strongly constrained by this latest data point, since it is the surface temperature once the crust and core are in thermal equilibrium. Moreover, our choice of light-element column depth is smaller than in Brown & Cumming (2009) (who use $10^9\,\mathrm{g\,cm^{-2}}$), the effect of which leads to a higher core temperature because the envelope is less opaque (Cumming et al., 2016). The 1, 2 and 3σ confidence regions of the parameter space can be seen in Figure 2.5.

We ran a second set of physical models that included a low thermal conductivity layer, which is consistent with nuclear pasta. A nuclear pasta phase is expected to exist at the base of neutron star crusts (e.g., see Horowitz et al., 2015, and references therein). Pons et al. (2013) suggested that the irregular shapes in the pasta would lead to low conductivity. Horowitz et al. (2015) showed that there could be defects in the pasta and suggested that they could act as scattering sites that would lower the thermal conductivity. We kept T_c, Q_{imp}, and Q_{sh} of the crust as free parameters. We added Q_{imp} of the pasta layer and the density of the transition to the pasta phase, ρ_{pasta}, as variable parameters. The pasta layer

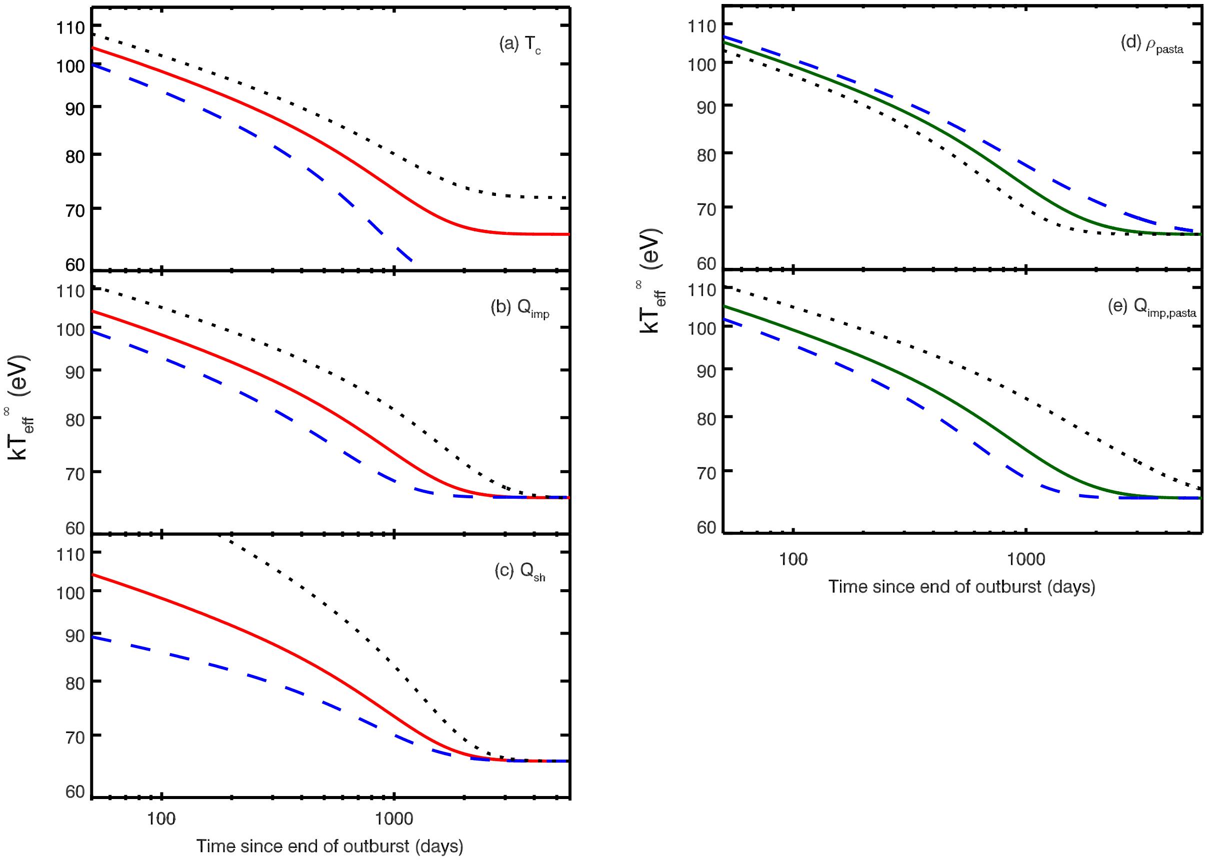

Figure 2.4: Influence of physical parameters in `dStar`. In panels $(a) - (c)$, the solid red line is the best fit model without a nuclear pasta layer. In panels $(d) - (e)$, the solid green line is the best fit model with nuclear pasta. In each panel we change only one parameter, while leaving the others at their best fit values. *(a)* the influence of changing the core temperature with dashed blue line showing $T_c = 7.35 \times 10^7$ K and dotted black line showing $T_c = 1.1 \times 10^8$ K. *(b)*, the influence of changing the impurity parameter, with dashed blue line showing $Q_{imp} = 1.0$ and dotted black line showing $Q_{imp} = 10.0$. *(c)* The influence of changing the amount of shallow heating with the dashed blue line showing $Q_{sh} = 0.60$ MeV/nucleon, and the dotted black line showing $Q_{sh} = 3.5$ MeV/nucleon. *(d)*, The influence of changing the transition density of the pasta with the dashed blue line showing $\rho_{\text{pasta}} = 1 \times 10^{13}$ g cm^{-3}, and the dotted black line showing $\rho_{\text{pasta}} = 6 \times 10^{13}$ g cm^{-3}. *(e)* The influence of changing the impurity parameter of the pasta, with the dashed blue line showing $Q_{imp,pasta} = 2.0$ and the dotted black line showing $Q_{imp,pasta} = 40$.

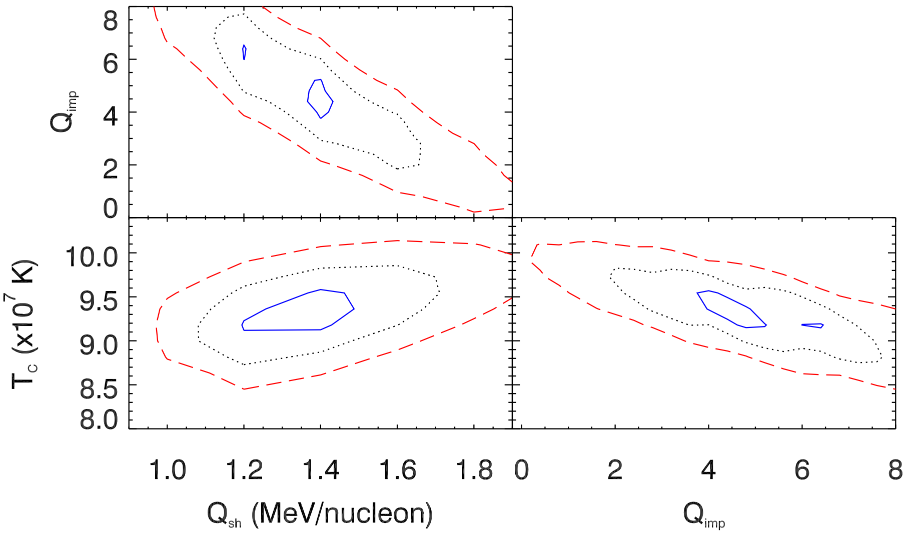

Figure 2.5: Contour plots of χ^2 distributions of the parameter space of the models without nuclear pasta. 1σ is designated by the solid blue line, 2σ by the dotted black line, and 3σ by the dashed red line.

is insulating. The presence of a pasta phase requires a greater temperature gradient to carry a thermal flux. As the transition density becomes smaller, the pasta layer becomes thicker, which causes the temperature of the crust to increase and the crust cools more slowly. Additionally, the pasta layer becomes more insulating as the impurity parameter is increased, resulting in a similar effect as the decreased transition density. The influence of the pasta parameters on the cooling curve can be seen in panels (d) – (e) of Figure 2.4. Again, we create a large grid of models, and find the model with the best (lowest) χ^2 value. The best fitting parameters are $T_c = 9.34 \pm 0.21 \times 10^7$ K, $Q_{imp} = 2.1 \pm 1.0$, $Q_{sh} = 1.43 \pm 0.15$ MeV/nucleon, $Q_{imp,pasta} = 12.4 \pm 5.1$, and $\rho_{pasta} = 2.7 \pm 0.8 \times 10^{13}$ g cm^{-3}. The best-fitting pasta model is shown as a dashed red line in Figure 2.6. This model gives a reduced-χ^2 = 3.232 (dof=3). The 1, 2 and 3 σ confidence regions of the parameter space can be seen in Figure 2.7.

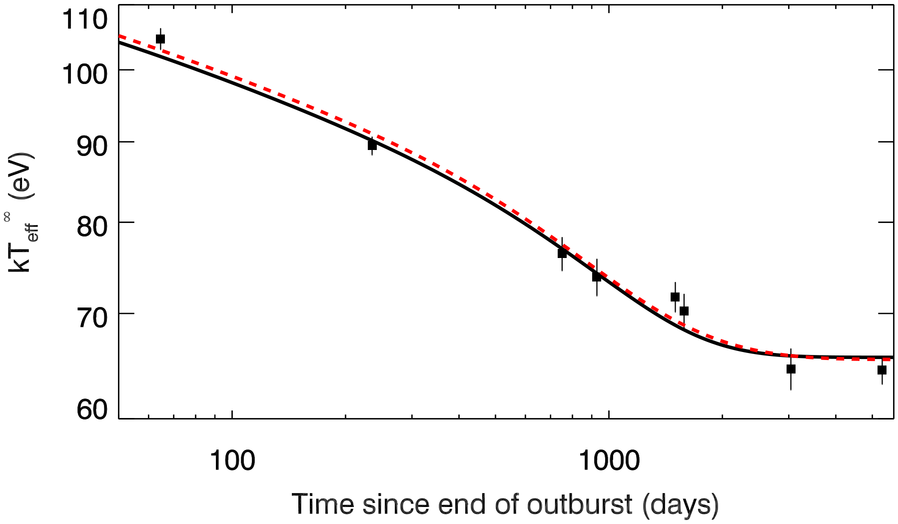

Figure 2.6: Comparison of best-fitting physical models from `dStar`. The solid black line is the best fit model without nuclear pasta., while the dashed red line is the best fit model including a nuclear pasta layer. Both cooling curves (with and without pasta) have similar shapes.

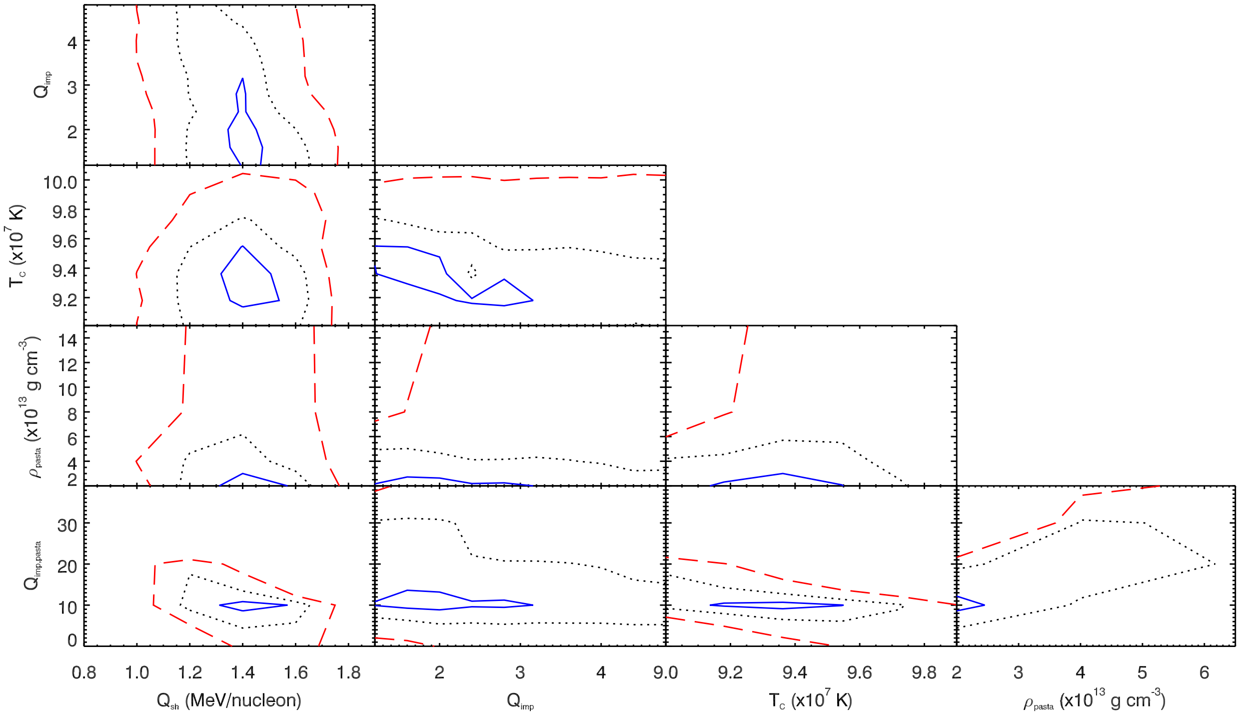

Figure 2.7: Contour plots of χ^2 distributions of the parameter space of the nuclear pasta models. 1σ is designated by the solid blue line, 2σ by the dotted black line, and 3σ by the dashed red line.

Chapter 3

Discussion and Future Work

3.1 Discussion

We have analyzed the newest *Chandra* observation of the neutron star LMXB KS 1731−260, 14.5 years into quiescence and six years after the previous *Chandra* observation. From fitting the X-ray spectrum we find an effective temperature of $kT_{\mathrm{eff}}{}^{\infty} = 64.4 \pm 1.2$ eV, which is consistent (within 1σ) of the 2009 *Chandra* observation which had $kT_{\mathrm{eff}}{}^{\infty} = 64.5 \pm 1.8$ eV, implying that the crust has likely thermally relaxed, and may have returned to equilibrium with the core. A broken power-law fits the cooling curve better than a simple power-law, at approximately the 3σ level. Alternatively, if we exclude the latest data point and re-fit a simple power-law decay we find that the newest observation is 3.5σ away from an extrapolation of the best-fitting model, further suggesting the crust has stopped cooling. We caution, however, that further observations are needed to confirm that this is not a deviation from the cooling curve caused by low-level accretion, as has been seen in, e.g., XTE J1701−462 (Fridriksson et al., 2011). The lack of a power-law component in the spectrum of this latest *Chandra* observation of KS 1731−260 suggests this may not be happening here.

We constrain crust properties using a physical model of the crust's thermal relaxation. This model calculates the thermal evolution of crust, and we initially allow the core temperature, impurity parameter and presence of additional shallow heat sources in the crust as free parameters to fit the cooling curve. We found best fit values for the core temperature and impurity parameter ($T_c = 9.35 \pm 0.25 \times 10^7$ K and $Q_{imp} = 4.4^{+2.2}_{-0.5}$). The low impurity parameter value is consistent with previous discussions that the crust of KS 1731−260 has high thermal conductivity (e.g., Wijnands et al., 2002; Cackett et al., 2006; Shternin et al., 2007; Brown & Cumming, 2009; Page & Reddy, 2013). The core temperature of the neutron star is most sensitive to cooling at late times. This new late time observation (~5300 days after the end of outburst), along with the full exploration of parameter space, places significantly improved constraints on the core temperature. In turn, constraints on the core temperature are important for placing a lower limit on the core's heat capacity (Cumming et al., 2016). Moreover, we find that significant additional shallow heat source in the crust is preferred, with a best-fitting value of $Q_{sh} = 1.36 \pm 0.18$ MeV/nucleon. This amount of extra heating is consistent with that found in other neutron star LMXBs (e.g., EXO 0748−676 and Aql X-1; Degenaar et al., 2014; Waterhouse et al., 2016), but is significantly less than the amount of shallow heating required for MAXI J0556−332 ($Q_{sh} \approx 4 - 10$ MeV/nucleon; Deibel et al., 2015).

`dStar` also allows to test for the presence of a layer of low thermal conductivity material close to the crust-core transition, possibly a nuclear pasta phase. However, we find that the inclusion of such a layer did not have significant influence on the best-fitting model, with the best fit coming from the lowest pasta density we allowed from the model (see contours in Figure 2.7). This is consistent with Horowitz et al. (2015) that KS 1731−260 can be modeled equally as well with or without a nuclear pasta layer. A parameter we did not vary in our pasta model was the superfluid critical temperature in the crust. In this analysis, we used the neutron superfluid critical temperature profile from Schwenk et al. (2003). Deibel et al. (2016) uses the superfluid critical temperature profile from Gandolfi et al. (2008). The difference between these two profiles is where the $^1S_0$ neutron pairing gap closes. In Schwenk et al. (2003), the pairing gap closes after the crust-core transition. In the profile from

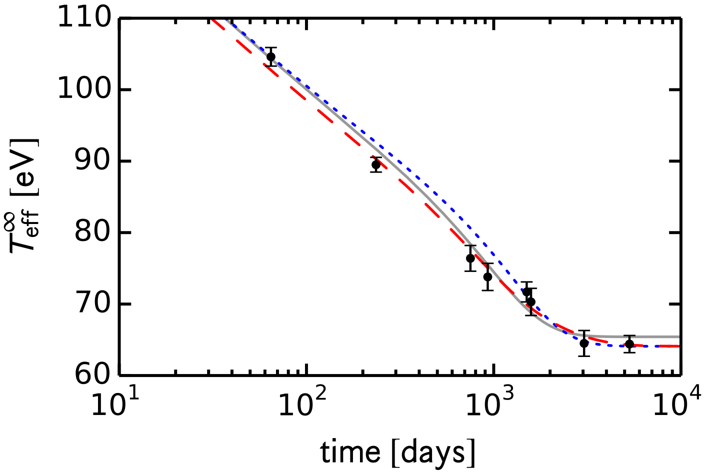

Figure 3.1: Comparison of physical models with varying impurity parameters and neutron superfluid critical temperature profile ($\mathrm{T_c}(\rho)$) from Deibel et al. (2016). The solid gray line is the best fit with no pasta from this analysis. The dotted blue line uses $\mathrm{T_c}(\rho)$ from Schwenk et al. (2003), T_c=9.1×10^7 K, $Q_{\rm imp}$= 2, and $Q_{\rm imp,pasta}$= 20. The red dashed line uses $\mathrm{T_c}(\rho)$ from Gandolfi et al. (2008), T_c=9.1×10^7 K, $Q_{\rm imp}$= 2, and $Q_{\rm imp,pasta}$= 20.

Gandolfi et al. (2008), the pairing gap closes in the inner crust. Using a neutron superfluid critical temperature profile that closes the $^1S_0$ neutron pairing gap prior to the crust-core transition does allow for the model to have a preference towards a layer of nuclear pasta. A comparison of models can be seen in Figure 3.1.

Our modeling with `dStar` assumes a constant accretion rate throughout the 12.5 year outburst of KS 1731−260. However, a recent investigation by Ootes et al. (2016) has shown that variations in the accretion rate throughout the outburst influences the cooling curve. Especially important are variations at the end of the outburst, which can strongly influence the early part of the cooling curve, and hence have a significant impact on the implied amount of extra heating at shallow depths. Their modeling of KS 1731−260 (without including the latest observation) finds the need for a 1.4 MeV/nucleon shallow heat source when variations in accretion rate are included and only 0.6 MeV/nucleon when a constant accretion rate is assumed (though, note, that Ootes et al. (2016) do not optimize their fits to get the best-fit parameters). This value for Q_{sh} is significantly less than the value implied from our modeling, suggesting some dependence on the input parameters that we do not fit for, such as the depth of the shallow heating and crust composition included in the cooling code. For instance, the minimum shallow heating density we use is $\rho_{sh,min} = 2.12 \times 10^9$ g cm^{-3}, while Ootes et al. (2016) use $\rho_{sh,min} = 4 \times 10^8$ g cm^{-3}. The choice of $\rho_{sh,min}$ was used in previous calculations and we have tested that our results are insensitive to the precise value.

KS 1731−260 has shown superbursts (Kuulkers et al., 2002), type-I X-ray bursts due to thermonuclear burning of carbon, leading to bursts that last for hours rather than tens of seconds. The conditions required for carbon to ignite places constraints on the thermal properties of the crust (Cumming et al., 2006), independently to the constraints placed by crustal cooling. The presence of superbursts requires that the crust has a temperature of $\sim 6 \times 10^8$ K at a depth of $\sim 10^{12}$ g cm^{-2} (Cumming et al., 2006). Without any additional heat source the crust is too cold (Cumming et al., 2006; Gasques et al., 2007). `dStar` gives the crust temperature profile at all times, thus we can study the temperature in the crust at the time of the superburst. As discussed in Ootes et al. (2016), the accretion rate during the outburst varies, and is significantly higher in the earlier part than at the end. The persistent flux before the superburst (taken from Kuulkers et al., 2002) is about 1.66 times higher than the average mass accretion rate we assume. We therefore recalculate the thermal evolution of the crust during the outburst assuming this higher mass accretion rate, and a correspondingly higher value of Q_{sh}, and look at the crust temperature profile at a time of 2894 days into the outburst (when the superburst took place). Doing this gives a temperature in the outer part of the crust (close to 10^{12} g cm^{-2}) of $\sim 5 \times 10^8$ K, which is broadly consistent with the required 6×10^8 K for superburst ignition, within the uncertainties and assumptions made.

3.2 Future Work

KS 1731−260 provides the rare opportunity to place two independent mass-radius constraints on the same source. During outburst, KS 1731−260 displayed photospheric radius expansion (PRE) bursts (Muno et al., 2000). PRE bursts are thought to reach the Eddington luminosity, thus fitting the blackbody emission from the burst can lead to both mass and radius constraints (both the Eddington luminosity and observed emitted radius depend on M and R), assuming the distance to the source is known (Özel 2006, though see e.g. Poutanen et al. 2014 for an opposing view). Özel et al. (2012) applied this technique to KS 1731−260, implying $R \leq 12.5$ km and $M \leq 2.1$ $\mathrm{M}_{\odot}$ (95% confidence level).

In future work, we will explore constraints on M and R through fitting crustal cooling models to KS 1731−260. Using Markov chain Monte Carlo (MCMC) methods, we want to constrain the mass and radius of KS 1731−260. We have an MCMC code capable of running 5-8 millions cooling curves a day to scan through these parameters. Determining M/R for a neutron star (it's 'compactness') is one of the ultimate goals for neutron star studies, since it has direct implications for the equation of state of ultra-dense matter in the neutron star core. Crustal cooling curves are sensitive to the neutron star compactness since the neutron star gravity influences the thickness of the crust. This, in turn, influences all length-scales in the cooling process, and hence, the shape of the cooling curve. KS 1731−260 provides a rare opportunity to explore what sort of constraints on M/R are possible from crustal cooling curves, and this will be an important next step.

Bibliography

Arnaud, K., Smith, R., & Siemiginowska, A., eds. 2011, Handbook of X-ray Astronomy, 1st edn. (The Edinburgh Building, Cambridge CB2 8RU, UK: Cambridge University Press)

Arnaud, K. A. 1996, in ASP Conf. Ser. 101: Astronomical Data Analysis Software and Systems V, 17

Bernardini, F., Cackett, E., Brown, E., D'Angelo, C., Degenaar, N., Miller, J., Reynolds, M., & Wijnands, R. 2013, Monthly Notices of the Royal Astronomical Society, 436, 2465

Bogdanov, S., Grindlay, J. E., & van den Berg, M. 2005, ApJ, 630, 1029

Brown, E. F. 2015, dStar: Neutron star thermal evolution code, Astrophysics Source Code Library, ascl:1505.034

Brown, E. F., Bildsten, L., & Rutledge, R. E. 1998, ApJ, 504, L95

Brown, E. F. & Cumming, A. 2009, ApJ, 698, 1020

Cackett, E. M., Brown, E. F., Cumming, A., Degenaar, N., Fridriksson, J. K., Homan, J., Miller, J. M., & Wijnands, R. 2013, ApJ, 774, 131

Cackett, E. M., Brown, E. F., Cumming, A., Degenaar, N., Miller, J. M., & Wijnands, R. 2010a, ApJ, 722, L137

Cackett, E. M., Brown, E. F., Miller, J. M., & Wijnands, R. 2010b, ApJ, 720, 1325

Cackett, E. M., Wijnands, R., Linares, M., Miller, J. M., Homan, J., & Lewin, W. H. G. 2006, MNRAS, 372, 479

Cackett, E. M., Wijnands, R., Miller, J. M., Brown, E. F., & Degenaar, N. 2008, ApJ, 687, L87

Campana, S., Colpi, M., Mereghetti, S., Stella, L., & Tavani, M. 1998, A&A Rev., 8, 279

Caplan, M. E. & Horowitz, C. J. 2016, ArXiv e-prints

Cumming, A., Brown, E. F., Fattoyev, F. J., Horowitz, C. J., Page, D., & Reddy, S. 2016, ArXiv e-prints

Cumming, A., Macbeth, J., in 't Zand, J. J. M., & Page, D. 2006, ApJ, 646, 429

Das, A. & Ferbel, T. 2003, Introduction to Nuclear and Particle Physics, 2nd edn. (27 Warren Street, Suite 401-402, Hackensack, NJ: World Scientific Publishing Co. Pte. Ltd.)

Degenaar, N., Brown, E. F., & Wijnands, R. 2011a, MNRAS, 418, L152

Degenaar, N., Medin, Z., Cumming, A., Wijnands, R., Wolff, M. T., Cackett, E. M., Miller, J. M., Jonker, P. G., Homan, J., & Brown, E. F. 2014, ApJ, 791, 47

Degenaar, N., Wijnands, R., Bahramian, A., Sivakoff, G. R., Heinke, C. O., Brown, E. F., Fridriksson, J. K., Homan, J., Cackett, E. M., Cumming, A., Miller, J. M., Altamirano, D., & Pooley, D. 2015, MNRAS, 451, 2071

Degenaar, N., Wijnands, R., Brown, E. F., Altamirano, D., Cackett, E. M., Fridriksson, J., Homan, J., Heinke, C. O., Miller, J. M., Pooley, D., & Sivakoff, G. R. 2013, ApJ, 775, 48

Degenaar, N., Wijnands, R., Wolff, M. T., Ray, P. S., Wood, K. S., Homan, J., Lewin, W. H. G., Jonker, P. G., Cackett, E. M., Miller, J. M., & Brown, E. F. 2009, MNRAS, 396, L26

Degenaar, N., Wolff, M. T., Ray, P. S., Wood, K. S., Homan, J., Lewin, W. H. G., Jonker, P. G., Cackett, E. M., Miller, J. M., Brown, E. F., & Wijnands, R. 2011b, MNRAS, 412, 1409

Deibel, A., Cumming, A., Brown, E. F., & Page, D. 2015, ApJ, 809, L31

Deibel, A., Cumming, A., Brown, E. F., & Reddy, S. 2016, ArXiv e-prints

Díaz Trigo, M., Boirin, L., Costantini, E., Méndez, M., & Parmar, A. 2011, A&A, 528, A150

Frank, J., King, A., & Raine, D. 2002, Accretion Power in Astrophysics, 3rd edn. (The Edinburgh Building, Cambridge CB2 8RU, UK: Cambridge University Press)

Fridriksson, J. K., Homan, J., Wijnands, R., Cackett, E. M., Altamirano, D., Degenaar, N., Brown, E. F., Méndez, M., & Belloni, T. M. 2011, ApJ, 736, 162

Fridriksson, J. K., Homan, J., Wijnands, R., Méndez, M., Altamirano, D., Cackett, E. M., Brown, E. F., Belloni, T. M., Degenaar, N., & Lewin, W. H. G. 2010, ApJ, 714, 270

Galloway, D. K., Muno, M. P., Hartman, J. M., Psaltis, D., & Chakrabarty, D. 2008, ApJS, 179, 360

Gandolfi, S., Illarionov, A. Y., Fantoni, S., Pederiva, F., & Schmidt, K. E. 2008, Physical Review Letters, 101, 132501

Gasques, L. R., Brown, E. F., Chieffi, A., Jiang, C. L., Limongi, M., Rolfs, C., Wiescher, M., & Yakovlev, D. G. 2007, Phys. Rev. C, 76, 035802

Haensel, P. & Zdunik, J. L. 1990, A&A, 227, 431

—. 2008, A&A, 480, 459

Heinke, C. O., Rybicki, G. B., Narayan, R., & Grindlay, J. E. 2006, ApJ, 644, 1090

Homan, J., Fridriksson, J. K., Wijnands, R., Cackett, E. M., Degenaar, N., Linares, M., Lin, D., & Remillard, R. A. 2014, ApJ, 795, 131

Horowitz, C. J., Berry, D. K., Briggs, C. M., Caplan, M. E., Cumming, A., & Schneider, A. S. 2015, Physical Review Letters, 114, 031102

Kobyakov, D. & Pethick, C. J. 2014, Physical Review Letters, 112, 112504

Kuulkers, E., in't Zand, J. J. M., van Kerkwijk, M. H., Cornelisse, R., Smith, D. A., Heise, J., Bazzano, A., Cocchi, M., Natalucci, L., & Ubertini, P. 2002, A&A, 382, 503

Lattimer, J. M. & Prakash, M. 2004, Science, 304, 536

Medin, Z. & Cumming, A. 2014, ApJ, 783, L3

Merritt, R. L., Cackett, E. M., Brown, E. F., Page, D., Cumming, A., Degenaar, N., Deibel, A., Homan, J., Miller, J. M., & Wijnands, R. 2016, ApJ, 833, 186

Muno, M. P., Fox, D. W., Morgan, E. H., & Bildsten, L. 2000, ApJ, 542, 1016

Ootes, L. S., Page, D., Wijnands, R., & Degenaar, N. 2016, MNRAS Letters, in press, arXiv:1606.01923

Özel, F. 2006, Nature, 441, 1115

Özel, F., Gould, A., & Güver, T. 2012, ApJ, 748, 5

Page, D. & Reddy, S. 2013, Physical Review Letters, 111, 241102

Pons, J. A., Viganò, D., & Rea, N. 2013, Nature Physics, 9, 431

Poutanen, J., Nättilä, J., Kajava, J. J. E., Latvala, O.-M., Galloway, D. K., Kuulkers, E., & Suleimanov, V. F. 2014, MNRAS, 442, 3777

Prakash, M., Reddy, S., Lattimer, J. M., & Ellis, P. J. 1996, Acta Physica Hungarica, 4, 271

Prialnik, D. 2010, An Introduction to the Theory of Stellar Structure and Evolution, 2nd edn. (The Edinburgh Building, Cambridge CB2 8RU, UK: Cambridge University Press)

Rutledge, R. E., Bildsten, L., Brown, E. F., Pavlov, G. G., Zavlin, V. E., & Ushomirsky, G. 2002, ApJ, 580, 413

Schneider, A. S., Berry, D. K., Briggs, C. M., Caplan, M. E., & Horowitz, C. J. 2014, Phys. Rev. C, 90, 055805

Schneider, A. S., Horowitz, C. J., Hughto, J., & Berry, D. K. 2013, Phys. Rev. C, 88, 065807

Schwenk, A., Friman, B., & Brown, G. E. 2003, Nuclear Physics A, 713, 191

Shternin, P. S., Yakovlev, D. G., Haensel, P., & Potekhin, A. Y. 2007, MNRAS, 382, L43

Sunyaev, R., Gilfanov, M., Churazov, E., Loznikov, V., Yamburenko, N., Skinner, G. K., Patterson, T. G., Willmore, A. P., Emam, O., Brinkman, A. C., Heise, J., Intzand, J., & Jager, R. 1990, Soviet Astronomy Letters, 16, 59

Sunyaev, R. et al. 1989, IAU Circ., 4839

Turlione, A., Aguilera, D. N., & Pons, J. A. 2015, A&A, 577, A5

Ushomirsky, G. & Rutledge, R. E. 2001, MNRAS, 325, 1157

Waterhouse, A. C., Degenaar, N., Wijnands, R., Brown, E. F., Miller, J. M., Altamirano, D., & Linares, M. 2016, MNRAS, 456, 4001

Wijnands, R., Guainazzi, M., van der Klis, M., & Méndez, M. 2002, ApJ, 573, L45

Wijnands, R., Homan, J., Miller, J. M., & Lewin, W. H. G. 2004, ApJ, 606, L61

Wijnands, R., Miller, J. M., Markwardt, C., Lewin, W. H. G., & van der Klis, M. 2001, ApJ, 560, L159

Wijnands, R., Nowak, M., Miller, J. M., Homan, J., Wachter, S., & Lewin, W. H. G. 2003, ApJ, 594, 952

Zavlin, V. E. & Pavlov, G. G. 2002, in Neutron Stars, Pulsars, and Supernova Remnants, ed. W. Becker, H. Lesch, & J. Trümper, 263

Zavlin, V. E., Pavlov, G. G., & Shibanov, Y. A. 1996, A&A, 315, 141

ABSTRACT

Crustal cooling in the neutron star low-mass X-ray binary KS 1731−260

by

Rachael L. Merritt

May 2017

Advisor:	Professor Edward Cackett
Major:	Physics
Degree:	Master of Science

Neutron stars in binary systems can undergo periods of accretion (outburst), where infalling material heats the crust of the star out of thermal equilibrium with the core. When accretion stops (quiescence), we can directly observe the thermal relaxation of the crust. Crustal cooling of accretion-heated neutron stars provides insight into the stellar interior of neutron stars. The neutron star X-ray transient, KS 1731−260, was in outburst for 12.5 years before returning to quiescence in 2001. Here, we present a 150 ks Chandra observation of KS 1731−260 taken in August 2015, about 14.5 years into quiescence. We find that the neutron star surface temperature is consistent with the previous observation, suggesting the crust has reached thermal equilibrium with the core. Using a theoretical thermal evolution code, we fit the observed cooling curves and constrain the core temperature, composition, and the required level of extra shallow heating.

Autobiographical Statement

Name: Rachael Lynn Merritt

Education:

M.S. Physics, Wayne State University, Detroit, Michigan, 2017

B.S. Physics, Wayne State University, Detroit, Michigan, 2015

B.A. Astronomy, Wayne State University, Detroit, Michigan, 2015

B.A. Classics, Wayne State University, Detroit, Michigan, 2015

Publications:

"The Thermal State of KS 1731−260 after 14.5 years in Quiescence", *The Astrophysical Journal*, Volume 833, Issue 2, article id. 186, 7 pp. (2016)

Wayne State University has set me on a path of science and outreach. While working on my undergraduate and Masters degrees I have been involved in research and construction projects. As an undergraduate, I worked on comparing properties of supernova host galaxies and helped construct amplifiers for detectors at BELLE II. My graduate research has focused on crustal cooling of neutron star low mass X-ray binary. Through my research, I have been able to present at conferences across the country and am a published author. I have also been involved in outreach at the WSU Planetarium since October 2011. This has allowed me to communicate the wonder and importance of science to all ages and people from all walks of life.

I will take the foundation I have built at Wayne State and continue to develop it as I begin my PhD in Astronomy at Georgia State University in Atlanta this fall.